A Current- and Speed-Loop Decoupling Controller for SPMSM Under Periodic Disturbances

Pengchong Chen, Ying Luo, He Gan, Yanhong Liu, *Member, IEEE*,
and Yangquan Chen, *Senior Member, IEEE*

***Abstract*—The current and speed dual-loop control strategy based on field-oriented control for surfaced permanent magnet synchronous motors (SPMSMs) is widely applied in high-performance industrial sectors. This article presents a systematic control framework for the SPMSM dual-loop that includes a resonant-model-based extended state observer and a feedback controller. The proposed control framework is shown to achieve decoupling control between servo (speed/current tracking) and regulation (aperiodic and periodic disturbances rejection) for the dual loop, meaning that the disturbance rejection performance can be independently improved without changing the tracking performance. Resonant-model-based extend state observer is proposed to estimate and compensate for both aperiodic and periodic disturbances, and the corresponding feedback controllers are designed for the inner current-loop and the outer speed-loop. Then, the disturbance rejection systematic analysis method and parameters tuning method are proposed. Compared with the optimal proportional–integral–resonant control and active disturbance rejection control methods, experimental results demonstrate that the proposed control strategy achieves better speed tracking and disturbance rejection performance, decoupling control performance between speed tracking and disturbance rejection, robustness to parameter mismatch, and better periodic disturbance rejection performance.**

***Index Terms*—Decoupling control, dual-loop control, frequency domain, resonant-model extended state observer (RMESO), speed ripple, surfaced permanent magnet synchronous motor (SPMSM).**

I. INTRODUCTION

SURFACED permanent magnet synchronous motors (SPMSMs) are widely accepted in motion control applications due to their compact structure, high power density, high air-gap flux density, and high efficiency. Currently, SPMSMs are extensively applied in various industrial sectors [1], [2] and the goal of these applications is to achieve excellent dynamic response and disturbance suppression performances. A typical dual-loop control method, consisting of an internal current-loop and an external speed-loop, is commonly used in SPMSM speed servo drive systems [3]. The response performance of each loop is influenced by various disturbances including aperiodic and periodic disturbances, such as current measurement errors [4], [5], cogging torque [6], [7], and flux harmonics [8], [9]. Thus, all these disturbances/uncertainties must be taken into account in the controller design for a dual loop to constrict negative effects.

The proportional–integral–derivative (PID) controller plays an absolutely dominant role in industrial service due to its simple structure and mature parameter tuning technology. However, the well-known internal tradeoff between servo and regulation in PID controller limits its control performance in both speed tracking and load disturbance rejection [10], [11]. To overcome this tradeoff, some tradeoff tuning methods based on a weighted performance degradation index have been proposed to meet user demands for better tracking performance or disturbance rejection performance [12], [13]. Additionally, two-degree-of-freedom control structures have been proposed to address the above tradeoff. One approach is that mixes a set-point filter with the PID controller [14]. The set-point filter aims to achieve better servo performance and PID controller guarantees the regulation performance. Another effective method is based on disturbance observers, which have been practiced in various advanced engineering systems. The disturbances/uncertainties can be estimated and compensated using the designed disturbance observers such as an equivalent-input-disturbance approach [15], [16], uncertainty and disturbance estimator [17], disturbance observer [18], generalized proportional–integral observer [19], [20], and extended state observer (ESO) [21], [22], [23], [24]. Although these disturbance-observer-based controllers are effective to some extent, the goal of decoupling control between servo and regulation has not been achieved.

In [25], a two-degree-of-freedom controller based on fractional-order PD (FOPD) and generalized ESO (GESO) was proposed for PMSM speed control. The speed tracking and

---

Manuscript received 17 November 2023; revised 26 January 2024; accepted 11 March 2024. Date of publication 14 March 2024; date of current version 19 April 2024. This work was supported in part by the China Postdoctoral Science Foundation under Grant 2023M743182, in part by the Key Scientific Research Foundation of the Higher Education Institutions of Henan Province under Grant 24A413008, and in part by the National Natural Science Foundation of China under Grant 51975234. Recommended for publication by Associate Editor K. Akatsu. *(Corresponding author: Ying Luo.)*

Pengchong Chen and Yanhong Liu are with the School of Electrical and Information Engineering, Zhengzhou University, Zhengzhou 450001, China (e-mail: pc_chen@zzu.edu.cn; liuyh@zzu.edu.cn).

Ying Luo is with the School of Automation Science and Engineering, South China University of Technology, Guangzhou 510641, China (e-mail: yingluosase@scut.edu.cn).

He Gan is with the School of Mechanical Science & Engineering, Huazhong University of Science and Technology, Wuhan 430074, China (e-mail: hegan@hust.edu.cn).

Yangquan Chen is with the Department of Mechanical Engineering, School of Engineering, University of California, Merced, Merced, CA 95343 USA (e-mail: ychen53@ucmerced.edu).

Color versions of one or more figures in this article are available at https://doi.org/10.1109/TPEL.2024.3377228.

Digital Object Identifier 10.1109/TPEL.2024.3377228

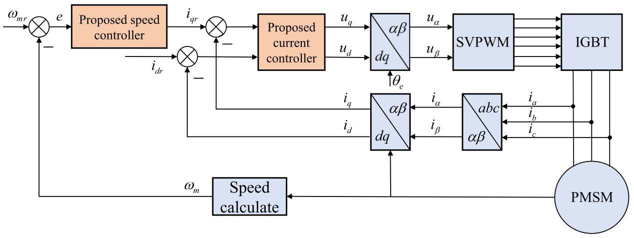

Fig. 1. Block diagram of SPMSM FOC control.

load-disturbance rejection performance had been achieved decoupling control through feedback FOPD controller and GESO. However, the periodic disturbances widely existing in PMSM were not considered, especially in low-speed operation. In recent years, scholars have done valuable work in dealing with periodic disturbances in the speed loop or the current loop of PMSM [26], [27], [28]. Tian et al. proposed adaptive resonant controllers based on ESO for the current loop [29] and speed loop [30] of PMSM to deal with uncertain periodic disturbances, respectively. The adaptive resonant controller is combined with the typical ESO in the current loop and is combined with PI controller in the speed loop. In [31], an enhanced ADRC with the quasi-resonant controller was proposed for the PMSM speed-loop to deal with aperiodic and periodic disturbances. The experimental results verified that the proposed controller can achieve smooth speed regulation compared with the PI controller and ADRC, but the current loop was not considered. In [32], an improved model predictive controller was proposed to enhance the suppression ability for periodic disturbances in the PMSM dual-loop. In [33], speed and current PIR control strategies were introduced for the PMSM dual-loop to minimize the periodic torque ripples due to harmonics of rotor flux, cogging torque, current measurement errors, and dead time of the inverter. The experiments were carried out to show that the proposed scheme can effectively suppress the speed ripples in a steady state. However, the resonant controller affected the open-loop frequency characteristics of the system and cannot achieve servo/regulation decoupling control.

Based on our previous work [25], we propose a resonant-model-ESO (RMESO) to tackle aperiodic and periodic disturbances in SPMSM dual-loop systems. The proposed control scheme combines RMESO and a feedback controller to achieve decoupling control between servo and regulation. The main contributions of this article are as follows.

1) A systematic control framework combining RMESO and feedback controller is proposed for the SPMSM dual-loop. RMESOs are designed to estimate and compensate aperiodic and periodic disturbances.
2) The proposed control scheme is verified to achieve decoupling control between servo and regulation, and a frequency-domain analysis method and a systemic design scheme based on the frequency-domain analysis for the proposed controllers in the dual loop are proposed.
3) The effectiveness of the proposed control scheme for the SPMSM dual-loop is validated through experimental results, compared with the proposed control methods in [33] and [21], which are also for the SPMSM dual-loop.

The rest of this article is organized as follows. Section II provides the background and preliminaries. The proposed controllers in the dual loop are given in Section III. Section IV presents the decoupling control verification, disturbance rejection analysis, and parameters tuning. Section V gives the experimental results. Finally, Section VI concludes this article.

II. BACKGROUND AND PRELIMINARIES

Fig. 1 shows the field-oriented control (FOC) strategy for SPMSM dual-loop control, where ω_{mr} is the reference speed, ω_m is the actual speed, e is the difference between reference speed and actual speed, i_{qr} is the reference current in the q-axis and i_{dr} is the reference current in the d-axis, u_q and u_d are the voltages of the q-axis and the d-axis, respectively, i_q and i_d are the actual current of the q-axis and the d-axis, respectively, and i_a, i_b, and i_c are the three-phase currents.

The electromagnetic and mechanical dynamics can be described as follows, with the hysteresis and eddy current loss, and the saturation nonlinear factor of the magnetization curve ignored.

A. Electromagnetic Dynamic

The current-loop dynamic model considering disturbances can be expressed as

$$\begin{aligned} \dot{i}_d &= \frac{1}{L}u_d - \frac{R}{L}i_d + \omega_e i_q + f_{\mathrm{ct}} \\ \dot{i}_q &= \frac{1}{L}u_q - \frac{R}{L}i_q - \omega_e i_d - \frac{1}{L}\omega_e\psi_f + f_{\mathrm{ct}} \end{aligned} \tag{1}$$

where i_d and i_q are the d-axis and the q-axis stator currents, u_d and u_q are the d-axis and q-axis stator voltages, ω_e is the electrical angular velocity, ψ is magnet flux linkage, f_{ct} is the total disturbances in the current loop, including flux harmonics, parameters uncertainty, and dead time effects. The disturbance analysis is provided in the Appendix. Note that the disturbances caused by flux harmonics and dead time effects are periodic, and the disturbance frequency is related to the motor speed.

With $i_d = 0$ control strategy in the FOC framework, the dynamic model of the q-axis can be presented as

$$\dot{i}_q = \frac{1}{L}u_q - \frac{R}{L}i_q + f_{\mathrm{ct}}. \tag{2}$$

The transfer function form can be expressed as

$$G_e = \frac{1}{Ls + R}. \tag{3}$$

B. Mechanical Dynamic

The speed-loop dynamic model considering disturbances can be expressed as

$$\begin{aligned} \dot{\omega_m} &= \frac{1}{J}T_e - f_{\mathrm{st}} \\ T_e &= 1.5p\psi i_q \end{aligned} \tag{4}$$

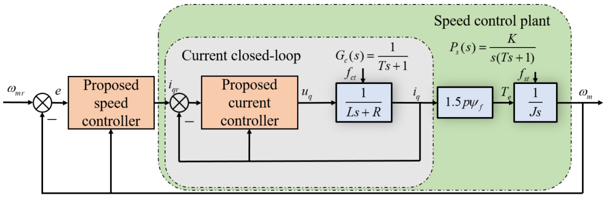

Fig. 2. Block diagram of the SPMSM dual-loop control system.

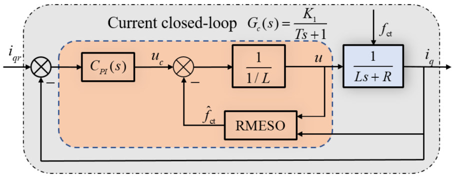

Fig. 3. Block diagram of the SPMSM current-loop control system based on the proposed current controller.

where ω_m is the mechanical angular speed, J is the inertia, T_e is the electromagnetic torque, f_{st} is the total disturbance in the speed loop, including flux harmonics, cogging torque, mechanical parameters uncertainty, and load torque, respectively, and p is the number of pole pairs. The disturbances due to flux harmonics and cogging torque are periodic, and the load torque is usually a constant disturbance. All the disturbance analyses are provided in the Appendix.

The transfer function form of mechanical dynamic can be expressed as

$$G_m = \frac{1.5p\psi}{Js}. \tag{5}$$

With the earlier analysis and Laplace transform, the block diagram of the SPMSM dual-loop control system with the proposed dual-loop controller is shown in Fig. 2

III. PROPOSED CONTROL SCHEME

A. Current-Loop Controller Design

The current-loop control plot can be shown in Fig. 3. The proposed controller includes an RMESO and a feedback controller.

1) RMESO Design: The state-space form of (2) is

$$\begin{bmatrix}\dot{i}_q\\ \dot{f}_{\text{ct}}\end{bmatrix} = \begin{bmatrix}-\frac{R}{L} & 1\\ 0 & 0\end{bmatrix}\begin{bmatrix} i_q\\ f_{\text{ct}}\end{bmatrix} + \begin{bmatrix}\frac{1}{L}\\ 0\end{bmatrix}u_q + \begin{bmatrix}0\\ 1\end{bmatrix}\dot{f}_{\text{ct}}. \tag{6}$$

To estimate the total disturbance f_{ct}, an RMESO is designed

$$\begin{bmatrix}\dot{\hat{i}}_q\\ \dot{\hat{f}}_{\text{ct}}\end{bmatrix} = \begin{bmatrix}-\frac{R}{L} & 1\\ 0 & 0\end{bmatrix}\begin{bmatrix}\hat{i}_q\\ \hat{f}_{\text{ct}}\end{bmatrix} + \begin{bmatrix}\frac{1}{L}\\ 0\end{bmatrix}u_q + \boldsymbol{L_c}[i_q - \hat{i}_q] \tag{7}$$

where $\boldsymbol{L_c} = [\beta_{\text{c1}} \;\; \beta_{\text{c2}}(1 + G_{\text{cr}}(s)s)]^{\text{T}}$, β_{c1} and β_{c1} are the observer gains, and $G_{\text{cr}}(s) = G_{\text{cr1}}(s) + G_{\text{cr2}}(s) + G_{\text{cr3}}(s)\cdots$. $G_{\text{cr}i}(s)$ is a resonant controller [34], which can deal with periodic disturbances. The proposed RMESO is presented in Fig. 4. The transfer function of the resonant controller is

$$G_{\text{cr}i}(s) = k_{ri}\frac{s\cos\phi - \omega_{ri}\sin\phi}{s^2 + \omega_{ri}^2} \tag{8}$$

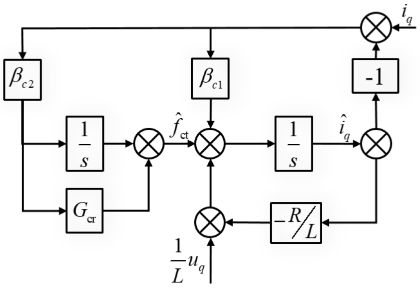

Fig. 4. Block diagram of RMESO.

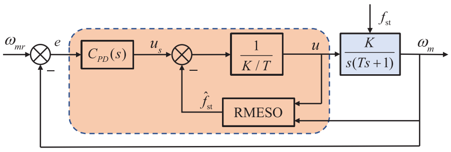

Fig. 5. Block diagram of the SPMSM speed-loop control system based on the proposed speed controller.

where k_{ri} is the resonant coefficient and ω_{ri} is the resonant frequency, and ϕ is the phase adjustment term.

Compared with traditional ESO, the proposed RMESO mainly includes two improvements: One is to make full use of model information to improve the antidisturbance capability of the observer, and the other is to include a resonance controller that can handle periodic disturbances.

2) Control Law Design: The control law is written as

$$u_q = \frac{u_c - \hat{f}_{\text{ct}}}{1/L} \tag{9}$$

where u_c is the output of the PI controller. The transfer function of the PI controller can be expressed as

$$C_{\text{PI}}(s) = K_{cp}\left(1 + \frac{K_{ci}}{s}\right) \tag{10}$$

where K_{cp} and K_{ci} are proportional and integral gains, respectively.

B. Speed-Loop Controller Design

The speed-loop control plot can be shown in Fig. 5.

1) RMESO Design: The speed control plant consists of the current closed-loop and mechanical dynamic model. The current closed-loop transfer function can be expressed as

$$G_c(s) = \frac{1}{Ts+1} \tag{11}$$

where $T = \frac{1}{K_p}$ and the derivation is given in Section IV-A.

Combining (5) and (11), the speed control plant can be obtained as

$$P_s(s) = \frac{Y(s)}{U(s)} = \frac{K}{s(Ts+1)} \tag{12}$$

where $K = 1.5\psi_f p/J$, and Y and U represent the motor speed and the output of speed controller, respectively.

The differential equation form of (12) can be obtained as

$$\ddot{y} = -\frac{1}{T}\dot{y} + \frac{K}{T}u - f_{\mathrm{st}}. \tag{13}$$

Define $\boldsymbol{z} = [z_1\ \ z_2\ \ z_3]^{\mathrm{T}} = [y\ \ \dot{y}\ \ f_{\mathrm{st}}]^{\mathrm{T}}$. Assume that f_{st} is differentiable and let $\dot{f}_{\mathrm{st}} = h$. Then, (13) can be rewritten as

$$\begin{aligned} \dot{\boldsymbol{z}} &= \boldsymbol{A}\boldsymbol{z} + \boldsymbol{B}u + \boldsymbol{E}h \\ y &= \boldsymbol{C}\boldsymbol{z} \end{aligned} \tag{14}$$

where $\boldsymbol{A} = \begin{bmatrix} 0 & 1 & 0 \\ 0 & -1/T & 1 \\ 0 & 0 & 0 \end{bmatrix}$, $\boldsymbol{B} = \begin{bmatrix} 0 \\ K/L \\ 0 \end{bmatrix}$, $\boldsymbol{E} = \begin{bmatrix} 0 \\ 0 \\ 1 \end{bmatrix}$, $\boldsymbol{C} = [1\ \ 0\ \ 0]$.

Consequently, the RMESO for the speed control plant is designed according to (14)

$$\begin{aligned} \dot{\hat{\boldsymbol{z}}} &= \boldsymbol{A}\hat{\boldsymbol{z}} + \boldsymbol{B}u + \boldsymbol{L_s}(y - \hat{y}) \\ \hat{y} &= \boldsymbol{C}\hat{\boldsymbol{z}} \end{aligned} \tag{15}$$

where $\boldsymbol{L_s} = [\beta_{\mathrm{s1}}\ \beta_{\mathrm{s2}}\ \beta_{\mathrm{s3}}(1 + G_{\mathrm{sr}}(s)s)]^{\mathrm{T}}$, $\beta_{\mathrm{s1}}, \beta_{\mathrm{s2}}, \beta_{\mathrm{s3}}$ are the observer gains, $G_{\mathrm{sr}}(s)$ are the resonant controller in the speed loop, $\hat{\boldsymbol{z}} = [\hat{z}_1\ \hat{z}_2\ \hat{z}_3]^{\mathrm{T}}$, $\hat{z}_1$ approximates y, $\hat{z}_2$ approximates $\dot{y}$, and $\hat{z}_3$ tracks f_{st}.

2) Control Law Design: The control law can be designed as

$$u = \frac{u_s - \hat{z}_3}{K/L} \tag{16}$$

where u_s is the output of the PD controller. The transfer function of the PD controller is

$$C_{\mathrm{PD}}(s) = K_{sp} + K_{sd}s \tag{17}$$

where K_{sp} and K_{sd} are proportional and differential gains, respectively.

IV. DECOUPLING CONTROL VERIFICATION, DISTURBANCE REJECTION ANALYSIS, AND PARAMETERS TUNING

A. Decoupling Control Verification

1) For Inner Current-Loop: According to (7), $F_{\mathrm{ct}}(s)$ can be calculated with the Laplace transform

$$\hat{F}_{\mathrm{ct}}(s) = \frac{\beta_{\mathrm{c2}}(1 + G_{\mathrm{cr}}(s)s)\left[(s + \frac{R}{L})i_q - \frac{1}{L}u_q\right]}{s^2 + \left(\frac{R}{L} + \beta_{\mathrm{c1}}\right)s + \beta_{\mathrm{c2}}(1 + G_{\mathrm{cr}}(s)s)}. \tag{18}$$

Next, combining (9) and (18), the transfer function from u_c to i_q can be expressed as

$$\begin{aligned} G_{\mathrm{cp}}(s) &= \frac{I_q(s)}{U_c(s)} \\ &= \frac{P_c(s)F(s)}{\frac{1}{L}F(s) + \beta_{\mathrm{c2}}(1 + G_{\mathrm{cr}}(s)s)\left(P_c(s)(s + \frac{R}{L}) - \frac{1}{L}\right)} \end{aligned} \tag{19}$$

where $P_c(s) = \frac{1}{Ls+R}$ is the transfer function of electromagnetic dynamic, $F(s) = s^2 + (\frac{R}{L} + \beta_{\mathrm{c1}})s + \beta_{\mathrm{c2}}(1 + G_{\mathrm{cr}}(s)s)$.

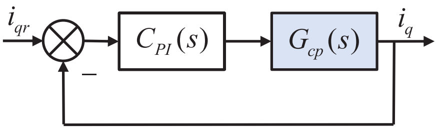

Fig. 6. Equivalent block diagram of the SPMSM current-loop control system.

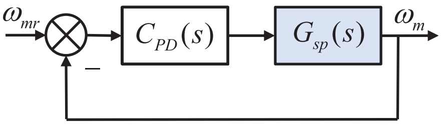

Fig. 7. Equivalent block diagram of the SPMSM speed-loop control system.

Substituting $P_c(s) = \frac{1}{Ls+R}$ into (19), yields

$$G_{cp}(s) = \frac{1}{s + \frac{R}{L}}. \tag{20}$$

Clearly, the equivalent transfer function from u_c to i_q through the designed RMESO is unrelated to the resonant controller, and the block diagram of current control system based on the proposed the current controller can be equivalent to Fig. 6. The servo performance is solely determined by the feedback controller. Thus, the open-loop and closed-loop transfer functions of the inner current-loop control system can be expressed as

$$G_{\mathrm{oc}}(s) = C_{\mathrm{PI}}(s)G_{cp}(s) \tag{21}$$

$$G_{\mathrm{c}}(s) = \frac{C_{\mathrm{PI}}(s)G_{cp}(s)}{1 + C_{\mathrm{PI}}(s)G_{cp}(s)}. \tag{22}$$

2) For Outer Speed-Loop: According to (15), $\hat{Z}_3(s)$ can be calculated with the Laplace transform

$$\hat{Z}_3(s) = \frac{\beta_{\mathrm{s3}}(1 + G_{\mathrm{sr}}(s)s)\left((s^2 + \frac{1}{T}s)\,Y(s) - \frac{K}{T}U(s)\right)}{E(s)} \tag{23}$$

where $E(s) = s^3 + (\frac{1}{T} + \beta_{\mathrm{s1}})s^2 + (\frac{1}{T}\beta_{\mathrm{s1}} + \beta_{\mathrm{s2}})s + \beta_{\mathrm{s3}}(1 + G_{\mathrm{sr}}(s)s)$.

Then, the transfer function from u_s to ω_m can be represented as

$$\begin{aligned} G_{sp}(s) &= \frac{\Omega_m(s)}{U_s(s)} \\ &= \frac{P_s(s)E(s)}{\frac{K}{T}E(s) + \beta_{\mathrm{s3}}(1 + G_{\mathrm{sr}}(s)s)(P_s(s)(s^2 + \frac{1}{T}s) - \frac{K}{T})}. \end{aligned} \tag{24}$$

Substituting (12) into (24), yields

$$G_{\mathrm{sp}}(s) = \frac{1}{s(s + \frac{1}{T})}. \tag{25}$$

Similarly, the equivalent transfer function from u_s to ω_m through the designed RMESO is nothing with the resonant controller and the block diagram of speed control system can be equated to Fig. 7. The servo performance is only determined by feedback controller $C_{\mathrm{PD}}(s)$. Thus, the open-loop and

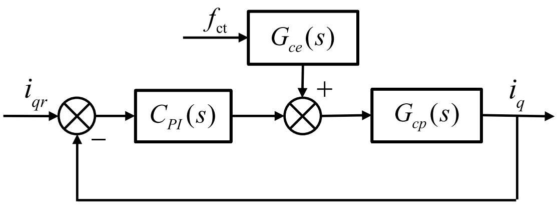

Fig. 8. Equivalent disturbance rejection block diagram of the SPMSM current-loop control system.

closed-loop transfer functions of the speed control system can be expressed as

$$G_{\rm os}(s) = C_{\rm PD}(s)G_{\rm sp}(s) \tag{26}$$

$$G_{\rm cs}(s) = \frac{C_{\rm PD}(s)G_{\rm sp}(s)}{1 + C_{\rm PD}(s)G_{\rm sp}(s)}. \tag{27}$$

In summary, both the proposed control schemes in the current loop and the speed loop can achieve servo/regulation decoupling control.

B. Disturbance Rejection Analysis

1) For Inner Current-Loop: The transfer function from total disturbance $f_{\rm ct}$ to the speed tracking error e is analyzed. Define $i_{qe} = i_q - \hat{i}_q$, $f_{\rm cte} = f_{\rm ct} - \hat{f}_{\rm ct}$, the estimation errors can be obtained

$$\begin{bmatrix} \dot{i}_{qe} \\ \dot{f}_{\rm cte} \end{bmatrix} = \begin{bmatrix} -\beta_{\rm c1} - \frac{R}{L} & 1 \\ -\beta_{\rm c2}(1 + G_{\rm cr}(s)s) & 0 \end{bmatrix} \begin{bmatrix} i_{qe} \\ f_{\rm cte} \end{bmatrix} + \begin{bmatrix} 0 \\ 1 \end{bmatrix} \dot{f}_{\rm ct}. \tag{28}$$

Then, the transfer function of total disturbance estimation error can be expressed as

$$G_{\rm ce}(s) = \frac{F_{\rm cte}(s)}{F_{\rm ct}(s)} = \frac{s^2 + (\beta_{\rm c1} + \frac{R}{L})s}{s^2 + (\beta_{\rm c1} + \frac{R}{L})s + \beta_{\rm c2}(1 + G_{\rm cr}(s)s)}. \tag{29}$$

From (2), the dynamic model of the q-axis can be equated to

$$\dot{i}_q = -\frac{R}{L}i_q + \frac{1}{L}\left(u_q + \frac{f_{\rm ct}}{1/L}\right). \tag{30}$$

Combining (9) and (30), yields

$$i_q = P_c(s)\frac{u_c - \hat{f}_{\rm ct}}{1/L} - \frac{f_{\rm ct}}{1/L} = G_{\rm cp}(s)(u_c + f_{\rm cte}). \tag{31}$$

According to (29) and (31), the equivalent current control block diagram can be represented as shown in Fig. 8. Therefore, the sensitivity transfer function of total disturbance $f_{\rm ct}$ to i_q tracking error can be calculated

$$E_c(s) = \frac{E_{iq}(s)}{F_{\rm ct}(s)} = \frac{G_{\rm ce}(s)G_{cp}(s)}{1 + C_{\rm PI}(s)G_{cp}(s)}. \tag{32}$$

2) For Outer Speed-Loop: Define $z_1 - \hat{z}_1 = e_{z1}$, $z_2 - \hat{z}_2 = e_{z2}$, and $z_3 - \hat{z}_3 = e_{z3}$. Subtracting (15) from (14), the estimation errors can be obtained

$$\begin{bmatrix} \dot{e}_{z1} \\ \dot{e}_{z2} \\ \dot{e}_{z3} \end{bmatrix} = \begin{bmatrix} -\beta_{\rm s1} & 1 & 0 \\ -\beta_{\rm s2} & -1/T & 1 \\ -\beta_{\rm s3}(1 + G_{\rm sr}(s)s) & 0 & 0 \end{bmatrix} \begin{bmatrix} e_{z1} \\ e_{z2} \\ e_{z3} \end{bmatrix} + \begin{bmatrix} 0 \\ 0 \\ 1 \end{bmatrix} h. \tag{33}$$

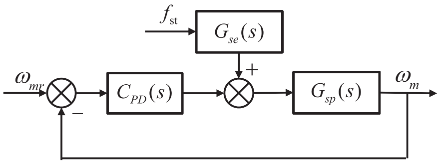

Fig. 9. Equivalent disturbance rejection block diagram of the SPMSM speed-loop control system.

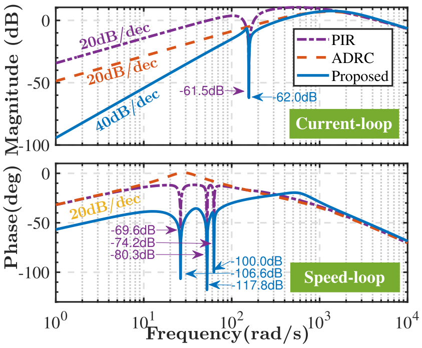

Fig. 10. Bode plots of sensitivity transfer functions of three control systems. Top: For current loop. Bottom: For speed loop.

Next, the transfer function of the total disturbance estimation error can be obtained

$$G_{\rm se}(s) = \frac{E_{z3}(s)}{F_{\rm st}} = \frac{s^3 + \left(\beta_{\rm s1} + \frac{1}{T}\right)s^2 + \left(\beta_{\rm s2} + \frac{1}{T}\beta_{\rm s1}\right)s}{s^3 + \left(\beta_{\rm s1} + \frac{1}{T}\right)s^2 + \left(\beta_{\rm s2} + \frac{1}{T}\beta_{\rm s1}\right)s + \beta_3(1 + G_{\rm sr}(s)s)}. \tag{34}$$

Similarly, the equivalent speed control block diagram can be expressed as shown in Fig. 9 and the sensitivity transfer function of disturbance $f_{\rm st}$ to ω tracking error can also be obtained

$$E_s(s) = \frac{E_{\omega m}(s)}{F_{\rm st}(s)} = \frac{G_{\rm se}(s)G_{sp}(s)}{1 + C_{\rm PD}(s)G_{sp}(s)}. \tag{35}$$

To show the advantages of the proposed control structure compared with the PIR controller [33] and ADRC [21], the Bode diagrams of sensitive functions including both current and speed loops for three control systems are shown in Fig. 10. All the controller parameters tuning methods are given in Section V-A. It can be seen from the top of Fig. 10 that the proposed controller for the current loop has the best low-frequency disturbance rejection performance with 40 dB/s. The other two controllers achieve the performance with 20 dB/s, but the ADRC has better performance with the designed controller parameters. In addition, PIR and the proposed controllers have a significant rejection ability for the periodic disturbance at the resonant frequency. For the speed loop, the frequency characteristics of PIR and ADRC have a small difference in low- and high-frequency bands, except at the resonant frequencies. However, the proposed controller achieves the best low-frequency disturbance rejection performance, and the rejection ability for the periodic disturbances outperforms the one of the PIR controller.

TABLE I
ROUTH ARRAY FOR RMESO IN CURRENT LOOP

s^4	1	b_2	b_4
s^3	b_1	b_3	
s^2	$\frac{b_1 b_2 - b_3}{b_1}$	b_4	
s^1	$\frac{(b_1 b_2 - b_3) b_3 - b_1^2 b_4}{b_1 b_2 - b_3}$		
s^0	b_4		

C. Stability Analysis

1) For RMESO: The stability can be evaluated by analyzing the root distribution of the characteristic polynomial of (29) and (34), using the Routh–Hurwitz stability criterion. In this section, the stability analysis is given in the case of the current loop.

According to (29), the characteristic polynomial can be expressed as

$$\lambda(s) = s^4 + \left(\beta_{c1} + \frac{R}{L}\right) s^3 + \left(\omega_{rc1}^2 + \beta_{c2} + k_{r1}\cos\phi\right) s^2 + \left(\omega_{rc1}^2 \left(\beta_{c1} + \frac{R}{L}\right) - \beta_{c2} k_{r1} \omega_{rc1} \sin\phi\right) s + \beta_{c2}\omega_{rc1}^2. \quad (36)$$

Substituting observer bandwidth ω_{co} (introduced in Section IV-D) into (36), $\lambda(s)$ can be derived as (37), and the Routh array is given in Table I

$$\lambda(s) = s^4 + b_1 s^3 + b_2 s^2 + b_3 s + b_4 \quad (37)$$

where

$$b_1 = 2\omega_{co}, b_2 = \omega_{rc1}^2 + \omega_{co}^2 + k_{r1}\omega_{co}^2 \cos\phi$$
$$b_3 = 2\omega_{rc1}^2 \omega_{co} - \omega_{co}^2 k_{r1} \omega_{rc1} \sin\phi, b_4 = \omega_{co}^2 \omega_{rc1}^2.$$

Thus, the conditions that must be satisfied for the stability of the MRESO in the current loop are given as

$$b_1 > 0, b_1 b_2 > b_3, (b_1 b_2 - b_3) b_3 - b_1^2 b_4 > 0, b_4 > 0. \quad (38)$$

Then, characteristic polynomial of RMESO in the speed loop is

$$\lambda(s) = s^5 + c_1 s^4 + c_2 s^3 + c_3 s^2 + c_4 s + c_5 \quad (39)$$

where

$$c_1 = 3\omega_{so}, c_2 = 3\omega_{so}^2 + \omega_{rs1}^2$$
$$c_3 = \omega_{so}^3 + 3\omega_{so}\omega_{rs1}^2 + k_{rs1}\omega_{so}^3 \cos\phi$$
$$c_4 = 3\omega_{so}^2 \omega_{rs1}^2 - k_{rs1}\omega_{so}^3 \sin\phi, c_5 = \omega_{so}^3 \omega_{rs1}^2.$$

The conditions that must be satisfied for the stability of the MRESO in the speed loop are given as

$$c_i > 0, (i = 1, 2, 3, 4, 5, c_1 c_2 c_3 > c_3^2 + c_1^2 c_4$$
$$(c_1 c_4 - c_5)(c_1 c_2 c_3 - c_3^2 - c_1^2 c_4) > c_5 (c_1 c_2 - c_3)^2 + c_1 c_5^2. \quad (40)$$

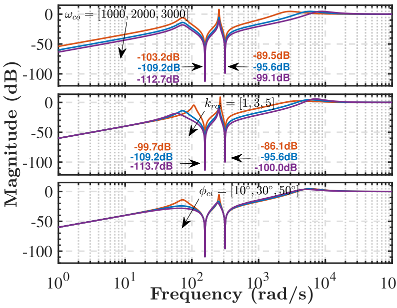

Fig. 11. Bode plots of disturbance estimation error with different parameters (Top: $\omega_{co} = 1000, 2000, 3000$. Middle: $k_{rci} = 1, 3, 5$. Bottom: $\phi_{ci} = 10°, 30°, 50°$).

2) For the Closed-Loop System: According to (10) and (20), the characteristic polynomial of the current closed-loop system can be calculated as

$$\lambda(s) = s^2 + \left(\frac{R}{L} + K_{cp}\right) + K_{cp} K_{ci}. \quad (41)$$

Thus, the conditions that must be satisfied for the stability of the current closed-loop system are given as

$$\frac{R}{L} + K_{cp} > 0, K_{cp} K_{ci} > 0. \quad (42)$$

Similarly, the characteristic polynomial of the speed closed-loop system can be calculated as

$$\lambda(s) = s^2 + \left(\frac{1}{T} + K_{sd}\right) s + K_{sp}. \quad (43)$$

Thus, the conditions that must be satisfied for the stability of the speed closed-loop system are given as

$$\frac{1}{T} + K_{sd} > 0, K_{sp} > 0. \quad (44)$$

D. Parameters Tuning

1) For Inner Current-Loop:

1) K_{cp}, K_{ci}: The parameters K_{ci} of the PI controller in the inner current-loop can be obtained through the "cancellation method" for the equivalent plant (20) [35], which is commonly used for the current-loop PI controller design, yields $K_{ci} = \frac{R}{L}$. K_{cp} can be determined with the gain crossover frequency $\omega_{\text{cgc}} = 400\pi$ rad/s according to the equation: $K_{cp} = \omega_{\text{cgc}}$.
2) β_{c1}, β_{c2}: The tuning of the observer gain vector guarantees the idea that place all the poles of MRESO to the same location $-\omega_{co}$, named as observer bandwidth. Thus, $\beta_{c1} = 2\omega_{co} - \frac{R}{L}$, $\beta_{c2} = \omega_{co}^2$. The Bode plots of total disturbance estimation error $G_{\text{se}}(s)$ with different bandwidths of RMESO are shown in Fig. 11. The magnitude is decreased gradually with the increase of ω_{co}. Theoretically, the disturbance rejection ability increases with increasing ω_{co}. However, the bandwidth is limited by sensor noises. Thus, ω_{co} is set as 2000 rad/s for the experiment in this article.
3) ϕ_{ci}, k_{rci}, ω_{rci}: In practical applications, one should determine which factor causes the larger disturbance to the system according to the analysis in the Appendix. Then, ω_{rci} equals the larger disturbance frequencies. The Bode

plots of $G_{\text{se}}(s)$ with different k_{rci} are shown in Fig. 11. Obviously, with the increasing of k_{rci}, the slot at the resonant frequencies is deeper, which means the ability improved to compensate periodic disturbances. Additionally, it can be observed that the magnitudes near the resonant frequencies spike, which will amplify disturbances at other frequencies. As k_{rci} increases, the magnitudes of the spikes at lower frequencies become smaller, but the magnitudes of the spikes at higher frequencies become larger. Therefore, the value of k_{rc1} not only affects the response at the resonant frequencies but also affects the response at near frequencies. A comprehensive consideration has been made to choose $k_{rc1} = 0.1$. The Bode plots of $G_{\text{se}}(s)$ with different ϕ_{ci} are shown in Fig. 11. It can be seen that the peaks can be suppressed with ϕ_{c1} increasing. Thus, ϕ_{c1} is set as $\frac{50\pi}{180}$ in this article.

2) For Outer Speed-Loop:

1) K_{sp}, K_{sd}: The parameters K_{sp} and K_{sd} can be determined with the frequency-domain specifications gain crossover frequency ω_{sgc} and phase margin ϕ_m. Given the frequency-domain specifications $\omega_{\text{sgc}} = 100$ rad/s, $\phi_{\text{sm}} = 80°$, controller parameters can be calculated as $K_{sp} = 1.2553 \times 10^5$ and $K_{sd} = -119.7950$.
2) β_{s1}, β_{s2}, β_{s3}: Similarly, observer gain vectors are determined by observer bandwidth ω_{so}, i.e., $\beta_{\text{s1}} = 3\omega_{so} - \frac{1}{T}$, $\beta_{\text{s2}} = 3\omega_{so}^2 - \frac{1}{T}\beta_{\text{s1}}$, and $\beta_{\text{s3}} = \omega_{so}^3$. ω_{so} is set as 500 rad/s for the experimental in this article.
3) ϕ_{si}, k_{rsi}, ω_{rsi}: ω_{rsi} equals the disturbance frequencies in the speed loop, which causes a larger speed ripple. According to the frequency-domain analysis with Bode plots in MATLAB, choose $k_{rs1} = 2$, $k_{rs2} = 2$, $k_{rs3} = 0.5$, $\omega_{rs1} = \frac{50\pi}{180}$, $\omega_{rs1} = \frac{90\pi}{180}$, $\omega_{rs1} = \frac{10\pi}{180}$.

E. Parameter Robustness Analysis

In practical applications, the parameter mismatch will diminish the control performance. Thus, the robustness analysis is given to evaluate the effects of gain variations on the closed-loop and disturbance rejection performance. The plant gain is set as $rb_s = 0.5, 1.0, 2.0$ times the normal value. Using the case speed-loop as an illustration, the Bode plots of the closed loop and the sensitivity transfer function are shown in Fig. 12.

According to the closed-loop Bode plot in Fig. 12, the purple line with resonant controllers (solid line) and without resonant controllers (dashed line) coincide if the model is accurate. Considering middle/high-speed operation, the resonant controllers are not deemed necessary due to the relatively small periodic disturbances. The plant gain variations impact the system bandwidth (-3 dB), but the system maintains no overshoot. Concerning disturbance rejection performance, as the plant gain increases, the speed drop becomes more pronounced. Considering low-speed operation, the resonant controller comes into effect. Similar to the case without the resonant controller, as the plant gain increases, the system bandwidth also increases, resulting in a shorter rise time. Conversely, with an increasing plant gain, the resonant frequency also increases, leading to a more pronounced reduction in speed.

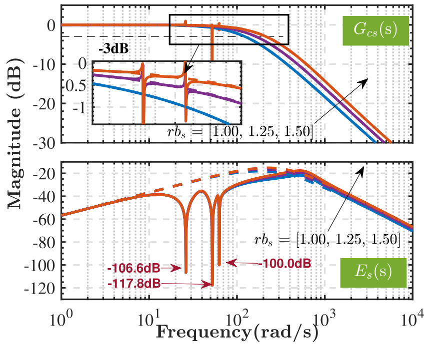

Fig. 12. Bode plots of the closed loop and the sensitivity transfer functions under different rb_s. Dashed line: Without resonant controllers. Solid line: With resonant controllers.

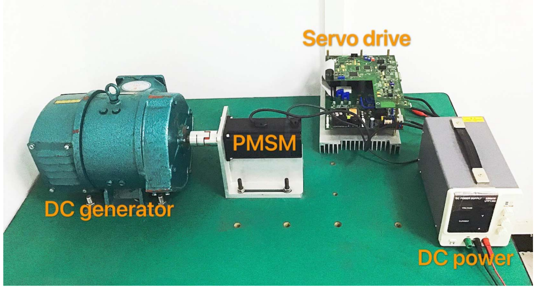

Fig. 13. SPMSM control platform.

TABLE II
PARAMETERS OF SPMSM

Parameter	Unit	Value
Inertia J	kg·m^2	24.3
Pole Pairs p	-	5
Slot s	-	12
Permanent fluxψ	Wb	0.82
Stator resistance R	Ω	0.46
Stator inductance L	mH	2.4
Rated speed	r/min	2000
Rated torque	N·m	9.5
Rated current	A	9.4
Rated voltage	V	220
Rated power	W	2000

V. EXPERIMENTAL VALIDATION

To demonstrate the efficiency of the proposed control strategy in the dual loop, experiments on the SPMSM current and speed servo systems are carried out. The experimental setup is shown in Fig. 13, which is composed of an SPMSM, a dc generator, a servo drive, and a PC. The model of the motor is VM7-M13A-2R020-D1 and parameters are listed in Table II. The self-developed servo drive is based on the TMS320F28335 digital signal processor (DSP), which is used for control algorithm implementation. The input command is given by the Ti Code Composer software (CCS) on PC and output data are sampled from encoder to servo drive by CCS. The insulated gate bipolar transistor power module PM100RLA060 is used as the power stage. The current

TABLE III
PARAMETERS OF THREE CONTROLLERS

Controller	Current loop	Speed loop
Proposed controller	$K_{cp} = 400\pi$, $K_{ci} = 190.9583$, $-R/L = -190.9583$ $\omega_{co} = 2000$, $\phi_{c1} = \frac{50\pi}{180}$, $k_{rc1} = 0.1$, $\omega_{rc1} = 6 \cdot \omega_{mr} \cdot p$	$K_{sp} = 1.2553 \cdot 10^5$, $K_{sd} = -119.7950$, $\omega_{so} = 500$ $\phi_{s1} = \frac{50\pi}{180}$, $k_{rs1} = 2$, $\omega_{rs1} = \omega_{mr} \cdot p$ $\phi_{s2} = \frac{90\pi}{180}$, $k_{rs2} = 2$, $\omega_{rs2} = 2 \cdot \omega_{mr} \cdot p$ $\phi_{s3} = \frac{10\pi}{180}$, $k_{rs3} = 0.5$, $\omega_{rs3} = s \cdot \omega_{mr}$
PIR	$K_{cp} = 3.0159$, $K_{ci} = 190.9583$ $\phi_{c1} = -\frac{40\pi}{180}$, $k_{rc1} = 40$, $\omega_{rc1} = 6 \cdot \omega_{mr} \cdot p$	$K_{sp} = 4.132$, $K_{si} = 9.5094$ $\phi_{s1} = \frac{0\pi}{180}$, $k_{rs1} = 20$, $\omega_{rs1} = \omega_{mr} \cdot p$ $\phi_{s2} = \frac{10\pi}{180}$, $k_{rs2} = 20$, $\omega_{rs2} = 2 \cdot \omega_{mr} \cdot p$ $\phi_{s3} = \frac{15\pi}{180}$, $k_{rs3} = 20$, $\omega_{rs3} = s \cdot \omega_{mr}$
ADRC	$\omega_{co} = 2000$, $\omega_{cc} = 400\pi$	$\omega_{so} = 500$, $\omega_{sc} = 100$

signal is collected by Hall current sensors (LTSR 6-NP). A 23-b absolute encoder is used to collect position and further calculate the speed. The sampling frequencies of the current loop and the speed loop are 10 kHz and 2 kHz, respectively.

A. *Parameters Design for PIR and ADRC Controllers*

For the fair comparison, the optimal PIR controller [33] and ADRC [21] are designed and tested on the dual-loop of SPMSM servo system for comparisons to verify the effectiveness of the proposed control strategy. The parameters tuning for the PIR controller is based on frequency-domain specifications gain crossover frequency and phase margin, which are the same as those for the proposed controller to keep fair comparison.

1) Parameters Design for PIR Controller: The parameters of the compared PI controller in the current loop are designed using the "cancellation method" for the plant (3) with the same gain crossover frequency, yields $K_{cp} = \omega_{\text{cgc}} L$ and $K_{ci} = \frac{R}{L}$. The parameters of the resonant controller are designed according to the method in [33]. The method for determining the resonant frequency is consistent with that employed in this article. The phase adjustment angle ϕ determines stability. The parameter ϕ is obtained through numerical simulations [33]. Large k_r results in good dynamic performance but reduces stable margin. A tradeoff has to be considered. Thus, the parameters of the resonant controller can be determined through some experiment tests. The controller parameters of the current loop are given in Table III. For the speed loop, one should calculate the transfer function of the controlled plant, which includes the closed loop of the current loop and the mechanical part. The calculated process can be referred to in our previous work [36]. The speed controlled plant can be expressed as

$$P(s) = \frac{b}{s(s+a)} \tag{45}$$

where $a = 1257$ and $b = 30\,380$.

The transfer function of the PI controller is

$$C(s) = K_{sp}\left(1 + \frac{K_{si}}{s}\right). \tag{46}$$

To obtain the PI controller parameters, two specifications concerned with the phase and gain of the open-loop transfer function are applied as follows.

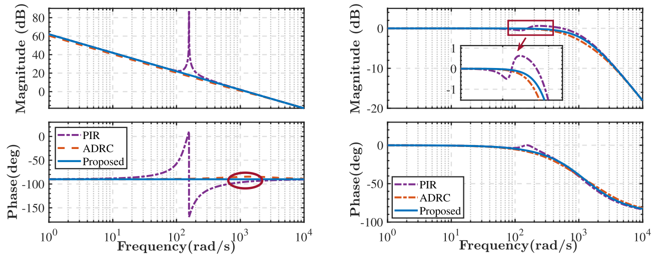

(a) (b)

Fig. 14. Open-loop and closed-loop Bode plots of three control systems for the current-loop system. (a) Open-loop Bode plots. (b) Closed-loop Bode plots.

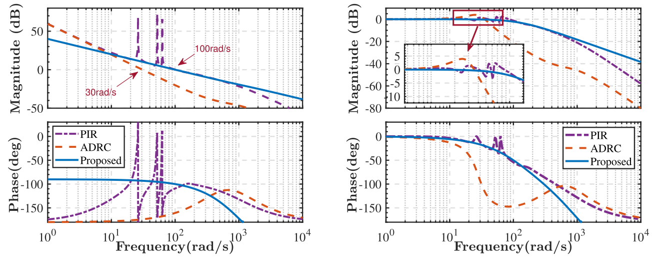

(a) (b)

Fig. 15. Open-loop and closed-loop Bode plots of three control systems for the speed-loop system. (a) Open-loop Bode plots. (b) Closed-loop Bode plots.

1) Specification on phase margin

$$-\tan\left(\frac{\omega_{\text{sgc}}}{a}\right) - \frac{\pi}{2} + \operatorname{atan}\left(-\frac{K_{si}}{\omega_{\text{sgc}}}\right) = -\pi + \phi_{\text{sm}}. \tag{47}$$

2) Specification on the gain crossover frequency

$$\frac{b}{\omega_{\text{sgc}}\sqrt{\omega_{\text{sgc}}^2 + a^2}} \cdot K_{sp}\sqrt{1 + \left(\frac{K_{si}}{\omega_{\text{sgc}}}\right)^2} = 1. \tag{48}$$

2) Parameters Design for ADRC: For the ADRC in the current and speed dual-loop system, the observer gains are consistent with that of the proposed controller. The controller bandwidths in the current and speed dual-loop are consistent with ω_{cgc} and ω_{sgc}. All the parameters have been summarized in Table III.

The open-loop and closed-loop Bode diagrams of three control systems for current and speed loops are shown in Figs. 14 and 15. It can seen from Fig. 14 that all three control systems

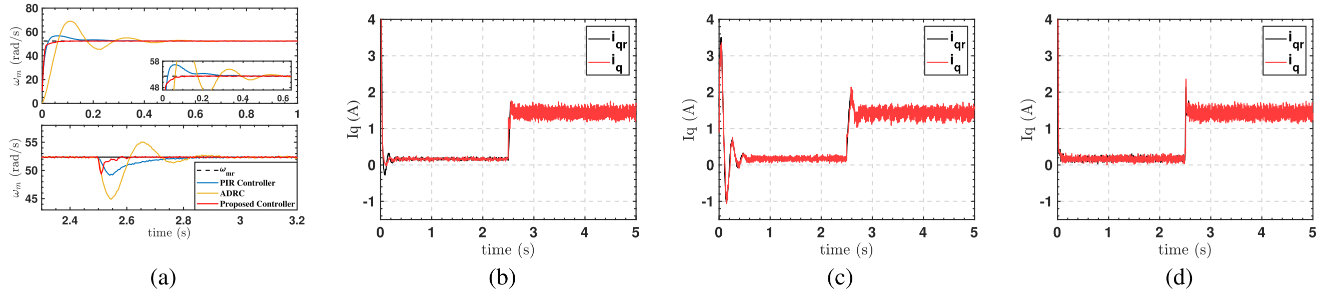

(a) (b) (c) (d)

Fig. 16. Speed responses and current responses for three control systems. (a) Speed tracking response comparison. (b) Current tracking performance of the PIR controller. (c) q-axis current tracking performance of ADRC. (d) q-axis current tracking performance of the proposed controller.

in the current loop satisfy the desired gain crossover frequency. The resonant controller in PIR reduces the phase margin in the open-loop Bode plot and increases the peak value in a closed-loop Bode plot, which will reduce the stability and increase overshoot for the system. From Fig. 15, the designed PIR controller and proposed controller basically satisfy the desired frequency-domain specifications. However, the gain crossover frequency of the designed ADRC control system is 30 rad/s, which is far from the desired gain crossover frequency of 100 rad/s. In fact, the desired gain crossover frequency for the ADRC system is based on the cascaded integrators ($\frac{1}{s^2}$), which should be achieved through the ESO. However, due to the internal dynamics $-as$, the model after estimating and compensating for the total disturbance of the ESO and cascaded integrators are significantly different.

B. Comparison Experiments

Six different experiments are carried out, which are given as follows.

1) The first one is to evaluate the step-speed tracking performance of the proposed control strategy.

   The reference speed is set as a step change signal of 0 to $\omega_{mr} = \frac{2\times\pi\times500\mathrm{r/min}}{60}$ rad/s$=$ 52.36 rad/s. Fig. 16(a) shows the experimental results of the speed tracking with three different control methods.

   As shown in Fig. 16(a), when the reference speed ω_{mr} is set as a step change signal of 0–52.36 rad/s (black dotted line), the actual speed using the PID controller (blue solid line) has a 4.3 rad/s (8%) overshoot and the settling time is 0.145 s. The yellow solid line shows the actual speed response using the ADRC in Fig. 16(a). It can be found that the overshoot is 16.66 rad/s (31.8%) and the settling time is 0.46 s. Obviously, the designed ADRC control system has a worse performance on step-speed tracking. The analysis is as follows: The effect of equivalent to the cascaded integrator by ESO is related to the bandwidth of ESO [37]. In this comparison, the bandwidth of ESO is the same as the bandwidth of the proposed RMESO, keeping a fair comparison. Indeed, the performance gets better if it increases the bandwidth of ESO in ADRC. However, the noise will also increase. The actual speed using the proposed controller (red solid line) has no overshoot and the settling time is 0.055 s. It can be clearly seen that the proposed controller achieves the best step-speed tracking performance with no overshoot and obviously shorter settling times than those of the PID controller and ADRC. The settling time represents the interval from the moment when the reference speed is given to that when the motor speed reaches within the error-tolerant range, within $\pm 2\%$ of the reference speed.

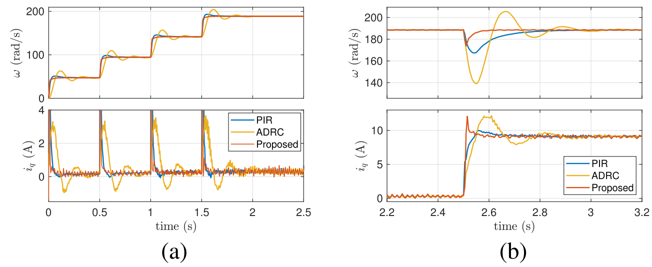

(a) (b)

Fig. 17. Speed responses and current responses. (a) Tracking performance within full speed range. (b) Rated speed and current responses.

2) The second one is to test the tracking performance within full speed range and response performance with rated speed and current.

   First, the reference speed is set as $\omega_{mr} = \frac{2\times\pi\times450/900/1350/1800\mathrm{r/min}}{60} = 47.124/94.248/141.371/$ 188.496 rad/s. The experimental comparison results including dynamic response and steady-state response with three designed controllers are shown in Fig. 17(a). The high speed with 188.496 rad/s and high-current with 8.86 A (in which both speed and current are close to the rated value) responses are shown in Fig. 17(b). The experimental results in Fig. 17(a) show that the proposed control strategy achieves better performance than the designed PI and ADRC within the full speed range. From Fig. 17(a), it can be seen that the proposed control strategy is effective with around rated speed and current.

3) The third one is to verify the decoupling control performance of the proposed control strategy.

   The reference speed is set as a step change signal of 0 to $\omega_{mr} = 52.36$ rad/s, with the observer bandwidth increasing from 300 rad/s to 500 rad/s. The experimental results of the speed tracking and load disturbance rejection performance are shown in Fig. 18. As shown in Fig. 18, the speed tracking performance has no change with different

TABLE IV
TIME-DOMAIN PERFORMANCE OF THREE CONTROL SYSTEMS

Controller	Velocity Tracking		Load disturbance rejection		Periodic disturbances rejection		
	Overshoot (%)	Settling time (s)	Speed drop (%)	Recovery time (s)	Speed ripple (rad/s)		
Proposed controller	0.00	0.055	3.00	0.02	±0.182	±0.157	±0.293
PIR	8.00	0.145	3.22	0.14	±0.405	±0.647	±1.565
ADRC	16.66	0.460	7.48	7.48	±0.853	±1.135	±2.402

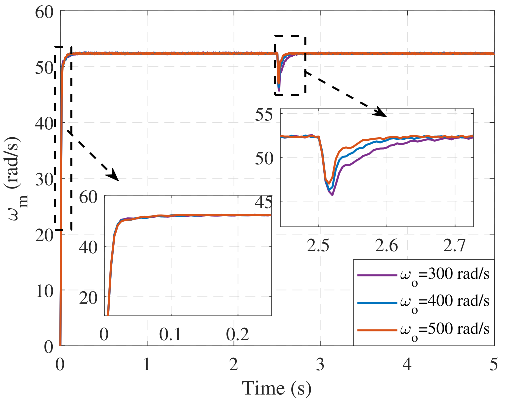

Fig. 18. Speed tracking and load disturbance rejection response with different observer bandwidths.

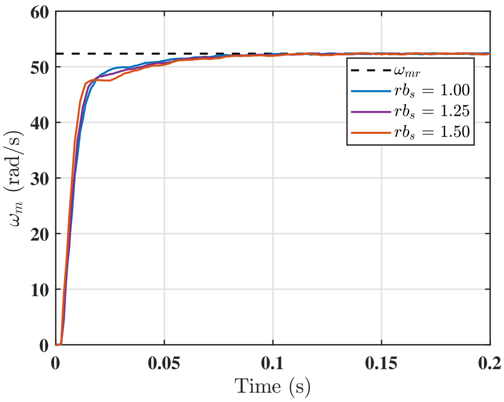

Fig. 19. Experimental results of robustness to plant parameter mismatch.

observer bandwidths, and only the load disturbance rejection performance gets better with the observer bandwidth increasing. Thus, the proposed control strategy verified the decoupling control performance in terms of speed tracking and load disturbance rejection.

4) The fourth one is to verify the step load torque rejection performance of the proposed control strategy.

   Injecting the load torque when the motor speed becomes stable at 2.5 s, Fig. 16(a) shows the experimental comparison results using three controllers. It can be seen in Fig. 16(a) that the designed PID controller has a 3.22 rad/s speed drop and the recovery time is 0.14 s. The designed ADRC achieves a 7.48 rad/s speed drop and the recovery time is 0.265 s. Compared with the designed PID and ADRC control systems, the speed drop of the proposed control system is reduced by 6.8% (from 3.22 to 3.0 rad/s) and 59.89% (from 7.48 to 3.0 rad/s), respectively. In terms of recovery time, the proposed control system is reduced by 85.71% (0.14–0.02 s) and 92.45% (0.265–0.02 s). The time-domain performance is summarized in Table IV. Thus, the proposed controller has a better load torque rejection performance than those of PID and ADRC.

5) The fifth one is to verify the performance of robustness to plant parameter mismatch of the proposed control strategy.

   The reference speed is set as a step change signal of 0 to $\omega_{mr} = 52.36$ rad/s, with the plant gain as kb_s= 1.00, 1.25, and 1.50 times the nominal value. The experimental results are shown in Fig. 19. From Fig. 19, with kb_s increasing, the rise time decreases and the overshoot keeps no change, which is consistent with theoretical analysis. Although the rise time of the responses has changed, this change is small enough, indicating that the proposed control system is robust to parameter mismatch.

6) The sixth one is to verify the current steady-state response with the periodic disturbance, dynamic response performance, and periodic disturbance rejection performance of the proposed control strategy at a low speed.

   The reference current is set as 2 A, and the q-axis current, A-phase current, and the FFT analysis of three designed control systems are presented in Fig. 20 from top to bottom, respectively. Using the ADRC method, it can be seen from Fig. 20(b) that the fluctuation of the q-axis current is 0.221 A, and the FFT analysis shows that the periodic disturbance due to dead time is obvious. Compared with the designed PIR control system, the proposed control system achieves better periodic disturbance rejection performance with current fluctuation of the q-axis is 0.182 A. The FFT analysis shows the same result with the time-domain response.

   The reference speed is set as $\omega_{mr} = \frac{2\times\pi\times30/40/50\,\mathrm{r/min}}{60}$ = 3.142/4.189/5.236 rad/s. The experimental comparison results (dynamic response performance and steady-state response performance) with three different control methods are shown in Fig. 21. Obviously, harsh speed ripples caused at a low speed can deteriorate the whole performance.

   First, it can be seen from the dynamic response in Fig. 21 that the proposed control strategy achieves the much better performance than others with no overshoot. The PIR controller achieves a little overshoot and the ADRC achieves the biggest overshoot. Then, according to the steady-state response in Fig. 21, the speed ripples using the proposed controller are smaller than those using the PIR

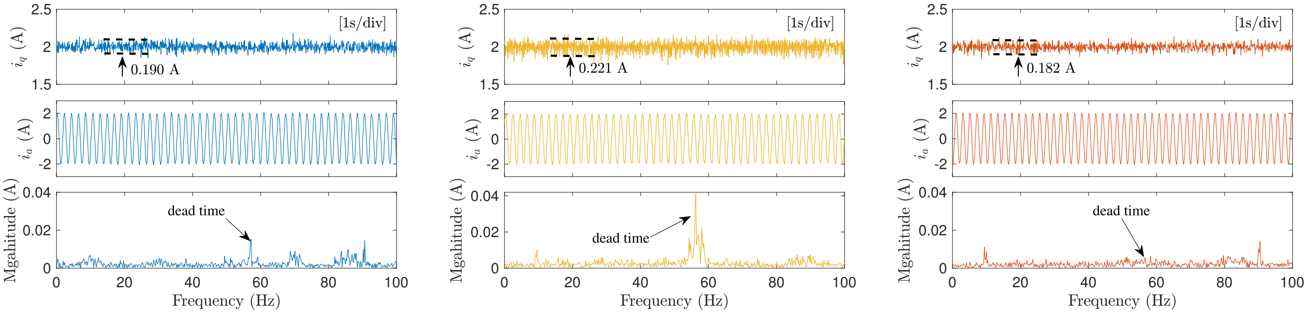

(a) (b) (c)

Fig. 20. Current responses of q-axis and A-phase and FFT analysis of three control systems. (a) PIR controller. (b) ADRC. (c) Proposed controller.

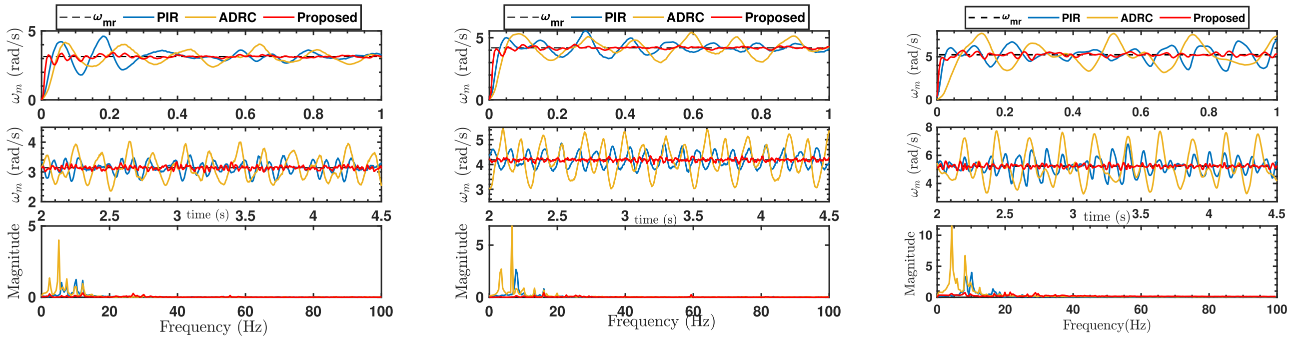

(a) (b) (c)

Fig. 21. Speed responses and FFT of three control systems with different reference speeds (Top: dynamic response; Middle: steady-state response; Bottom: FFT). (a) 3.142 rad/s. (b) 4.189 rad/s. (c) 5.236 rad/s.

controller and ADRC in different reference speeds. The speed ripples using the PIR controller, ADRC, and the proposed controller in different reference speeds are summarized in Table IV. Obviously, the proposed controller can achieve better dynamic response performance and steady-state response performance than those of ADRC and the PIR controller. To clearly analyze the factors of fluctuations, fast Fourier transformation (FFT) is utilized and the results are shown at the bottom of Fig. 21. Fig. 21 also shows that the ADRC control system has significant speed ripple and is not sufficiently efficient for periodic disturbances. The reason is that ADRC lacks an internal model of the periodic disturbances. It is worth noting that the high-frequency (30–100 Hz) response is worse with the proposed controller. This is because the "waterbed effect" in a control system. This question can be addressed with the proposed method in [38].

VI. CONCLUSION

In this article, a systematic control framework is proposed for the SPMSM dual-loop to attenuate both aperiodic and periodic disturbances. The proposed framework effectively suppresses the aperiodic and periodic disturbances by the RMESO. Through mathematical derivation and theoretical analysis, it is verified that the resonant controller does not affect the open-loop frequency characteristics. Thus, the proposed control framework achieves decoupling control, adjusting the parameters of the RMESO to improve the regulation performance without affecting the servo performance. The disturbance rejection frequency-domain analysis and parameters tuning method are given. Compared with the optimal PIR controller and ADRC, the proposed controller not only largely improves step-speed tracking and load disturbance rejection performances but also significantly reduces speed ripple due to extensive disturbances at a low speed.

APPENDIX

A. Disturbances in Current Loop

1) Flux Harmonics: In the ideal SPMSM, permanent magnet fluxes keep constant. However, due to manufacturing restrictions and the resultant demagnetization phenomenon of permanent magnets because of temperature, it is difficult to realize ideal sinusoidal flux density distribution. Thus, harmonics will exist in a practical SPMSM and it can be expressed as

$$\psi_f = \sum_{n=0}^{\infty} \psi_{fn} \cos\left(6n\theta_e\right) \tag{49}$$

where θ_e is the electrical angle, ψ_{fn} is the amplitude of the $6n$th-order harmonic flux, and n is a positive integer.

2) Dead Time Effects: To prevent short circuit of a dc link, dead time must exist in drive signals between upper and lower legs of each phase for space vector pulse width modulation voltage source inverter. The disturbance due to dead time effects on stator voltage can be expressed as

$$f_{\text{dead}} = \sum_{i=0}^{\infty} f_n \sin(6n\theta_e) \tag{50}$$

where f_n is the amplitude of the $6n$th-order harmonic disturbance.

3) Current Measurement Errors: The current measurement process includes sampling by Hall sensors, low-pass filtering, polarity conversion, analog/digital (A/D) converters, and calculation. Current measurement errors include offset error, which results from the residual current of current sensors or drift phenomena or operational amplifiers and A/D converters, and scaling error, which is mainly caused by the matching circuit between the current sensor and A/D input. The equivalent disturbances on the q-axis can be modeled as

$$\begin{aligned} i_q^{\text{offset}} &= i^{\text{offset}} \cos(\theta_e + \alpha), \\ i_q^{\text{scaling}} &= i^{\text{scaling}} \left[\sin(2\theta_e + \beta) - \frac{1}{2}\right] \end{aligned} \tag{51}$$

where i_q^{offset} and i_q^{scaling} are the disturbances due to offset and scaling, respectively, i^{offset} and i^{scaling} are the amplitude of ripples, and α and β are determined by the angle between the rotor position and stator current vector.

4) Electrical Parameters Uncertainty: Electrical parameters include stator resistance R and stator inductance L. Both of them are time varying in practical cases: R varies with temperature and L varies with time because of the effects of cross saturation. Thus, the disturbance f_{epu} due to parameters uncertainty exists in the current loop.

B. Disturbances in Speed Loop

1) Cogging Torque: Cogging torque is generated by the interaction between the permanent magnet and stator core and is caused by the tangential component of the interaction force between the permanent magnet and the armature teeth. Cogging torque still exists when the SPMSM is disconnected from the power source and it can be expressed as

$$f_{\text{cog}} = \sum_{n=1}^{\infty} f_n \sin(nN_c\theta_e/p) \tag{52}$$

where p is a number of motor pole pairs, N_c is the least common multiple between the number of slots and pole pairs, f_n is the amplitude of the nth component of the Fourier series.

2) Friction Torque: Friction is the resistance to motion when two surfaces slide against each other. Friction includes presliding region and sliding region and behaves hysteresis with nonlocal memory, Stribeck effect, and friction lag characteristics. So far, various models have been proposed to describe friction phenomenon: Dahl model [39], LuGre model [40], and generalized Maxwell-slip (GMS) model [41]. The GMS model can capture most the typical friction characteristics and it can be expressed as

$$F_f(t) = \sum_{n=1}^{N} F_n(t) + \sigma v(t) \tag{53}$$

where N represents the GMS model that includes N elementary state models, σ is the viscous friction coefficient, $v(t)$ represents speed, $F_n(t)$ has different equation form in different region: 1) in the presliding region, $\frac{dF_n}{dt} = k_n v(t)$, where k_n is the elementary stiffness value; 2) in the sliding region: $\frac{dF_n}{dt} = \text{sgn}(v)C(\alpha_i - \frac{F_n}{s(v)})$, where C is the attraction parameter, a_n is the fractional parameter, and $s(v)$ represents the Stribeck curve.

3) Mechanical Parameters Uncertainty: In many applications of SPMSM, for example, industrial robotic arms, the inertia J of the SPMSM system is time-varying because the position and attitude of the robot arm have changed. Thus, the disturbance f_{mpu} due to parameter uncertainty exists in the speed loop.

4) Load Torque: Load disturbance f_{load} is the most serious disturbance in the SPMSM system. Actual speed will fluctuate dramatically when a load disturbance is imposed on or evacuated from the SPMSM.

REFERENCES

[1] Y.-j. Wu and G.-f. Li, "Adaptive disturbance compensation finite control set optimal control for PMSM systems based on sliding mode extended state observer," *Mech. Syst. Signal Process.*, vol. 98, pp. 402–414, 2018.

[2] Z. Qiu, Y. Chen, Y. Kang, X. Liu, and F. Gu, "Investigation into periodic signal-based dithering modulations for suppression sideband vibro-acoustics in PMSM used by electric vehicles," *IEEE Trans. Energy Convers.*, vol. 36, no. 3, pp. 1787–1796, Sep. 2021.

[3] Z. Song, Y. Wang, and T. Shi, "A dual-loop predictive control structure for permanent magnet synchronous machines with enhanced attenuation of periodic disturbances," *IEEE Trans. Power Electron.*, vol. 35, no. 1, pp. 760–774, Jan. 2020.

[4] Q. Zhang et al., "Robust plug-in repetitive control for speed smoothness of cascaded-PI PMSM drive," *Mech. Syst. Signal Process.*, vol. 163, 2022, Art. no. 108090.

[5] Q. N. Trinh, P. Wang, Y. Tang, L. H. Koh, and F. H. Choo, "Compensation of DC offset and scaling errors in voltage and current measurements of three-phase AC/DC converters," *IEEE Trans. Power Electron.*, vol. 33, no. 6, pp. 5401–5414, Jun. 2018.

[6] A. Arias, J. Caum, E. Ibarra, and R. Griñó, "Reducing the cogging torque effects in hybrid stepper machines by means of resonant controllers," *IEEE Trans. Ind. Electron.*, vol. 66, no. 4, pp. 2603–2612, Apr. 2019.

[7] J. Ou, Y. Liu, R. Qu, and M. Doppelbauer, "Experimental and theoretical research on cogging torque of PM synchronous motors considering manufacturing tolerances," *IEEE Trans. Ind. Electron.*, vol. 65, no. 5, pp. 3772–3783, May 2018.

[8] Z. Pan, F. Dong, J. Zhao, L. Wang, H. Wang, and Y. Feng, "Combined resonant controller and two-degree-of-freedom PID controller for PMSLM current harmonics suppression," *IEEE Trans. Ind. Electron.*, vol. 65, no. 9, pp. 7558–7568, Sep. 2018.

[9] M. Ruderman and T. Bertram, "Variable proportional-integral-resonant (PIR) control of actuators with harmonic disturbances," in *Proc. IEEE Int. Conf. Mechatronics*, 2013, pp. 847–852.

[10] S. Alcántara, R. Vilanova, and C. Pedret, "PID control in terms of robustness/performance and servo/regulator trade-offs: A unifying approach to balanced autotuning," *J. Process Control*, vol. 23, no. 4, pp. 527–542, 2013.

[11] V. Alfaro, R. Vilanova, V. Méndez, and J. Lafuente, "Performance/robustness tradeoff analysis of PI/PID servo and regulatory control systems," in *Proc. IEEE Int. Conf. Ind. Technol.*, 2010, pp. 111–116.

[12] O. Arrieta, A. Visioli, and R. Vilanova, "PID autotuning for weighted servo/regulation control operation," *J. Process Control*, vol. 20, no. 4, pp. 472–480, 2010.

[13] C. Grimholt and S. Skogestad, "Optimal PI-control and verification of the SIMC tuning rule," *IFAC Proc. Vol.*, vol. 45, no. 3, pp. 11–22, 2012.

[14] S. Srivastava and V. Pandit, “A 2-Dof LQR based PID controller for integrating processes considering robustness/performance tradeoff,” *ISA Trans.*, vol. 71, pp. 426–439, 2017.

[15] J. She, K. Miyamoto, Q.-L. Han, M. Wu, H. Hashimoto, and Q.-G. Wang, “Generalized-extended-state-observer and equivalent-input-disturbance methods for active disturbance rejection: Deep observation and comparison,” *IEEE/CAA J. Automatica Sinica*, vol. 10, no. 4, pp. 957–968, Apr. 2023.

[16] X. Yin, Y. Shi, J. She, and H. Wang, “Equivalent input disturbance-based control: Analysis, development, and applications,” *IEEE Trans. Cybern.*, vol. 54, no. 4, pp. 2654–2667, 2024, doi: 10.1109/TCYB.2023.3306879.

[17] B. Ren, Q.-C. Zhong, and J. Chen, “Robust control for a class of nonaffine nonlinear systems based on the uncertainty and disturbance estimator,” *IEEE Trans. Ind. Electron.*, vol. 62, no. 9, pp. 5881–5888, Sep. 2015.

[18] E. Sariyildiz and K. Ohnishi, “Stability and robustness of disturbance-observer-based motion control systems,” *IEEE Trans. Ind. Electron.*, vol. 62, no. 1, pp. 414–422, Jan. 2015.

[19] J. Wang, F. Wang, G. Wang, S. Li, and L. Yu, “Generalized proportional integral observer based robust finite control set predictive current control for induction motor systems with time-varying disturbances,” *IEEE Trans. Ind. Informat.*, vol. 14, no. 9, pp. 4159–4168, Sep. 2018.

[20] J. Cheng, L. Liang, H. Yan, J. Cao, S. Tang, and K. Shi, “Proportional-integral observer-based state estimation for Markov memristive neural networks with sensor saturations,” *IEEE Trans. Neural Netw. Learn. Syst.*, vol. 35, no. 1, pp. 405–416, Jan. 2024, doi: 10.1109/TNNLS.2022.3174880.

[21] H. Sira-Ramírez, J. Linares-Flores, C. García-Rodríguez, and M. A. Contreras-Ordaz, “On the control of the permanent magnet synchronous motor: An active disturbance rejection control approach,” *IEEE Trans. Control Syst. Technol.*, vol. 22, no. 5, pp. 2056–2063, Sep. 2014.

[22] B.-Z. Guo and Z.-l. Zhao, “On the convergence of an extended state observer for nonlinear systems with uncertainty,” *Syst. Control Lett.*, vol. 60, no. 6, pp. 420–430, 2011.

[23] Y. Huang, W. Xue, G. Zhiqiang, H. Sira-Ramirez, D. Wu, and M. Sun, “Active disturbance rejection control: Methodology, practice and analysis,” in *Proc. 33rd Chin. Control Conf.*, 2014, pp. 1–5.

[24] P. Li, L. Wang, B. Zhong, and M. Zhang, “Linear active disturbance rejection control for two-mass systems via singular perturbation approach,” *IEEE Trans. Ind. Informat.*, vol. 18, no. 5, pp. 3022–3032, May 2022, doi: 10.1109/TII.2021.3108950.

[25] P. Chen and Y. Luo, “A two-degree-of-freedom controller design satisfying separation principle with fractional-order PD and generalized ESO,” *IEEE/ASME Trans. Mechatronics*, vol. 27, no. 1, pp. 137–148, Feb. 2022.

[26] S. Chai, L. Wang, and E. Rogers, “A cascade MPC control structure for a PMSM with speed ripple minimization,” *IEEE Trans. Ind. Electron.*, vol. 60, no. 8, pp. 2978–2987, Aug. 2013.

[27] J. Liu, H. Li, and Y. Deng, “Torque ripple minimization of PMSM based on robust ILC via adaptive sliding mode control,” *IEEE Trans. Power Electron.*, vol. 33, no. 4, pp. 3655–3671, Apr. 2018.

[28] F. Yang et al., “Complex coefficient active disturbance rejection controller for current harmonics suppression of IPMSM drives,” *IEEE Trans. Power Electron.*, vol. 37, no. 9, pp. 10443–10454, Sep. 2022.

[29] M. Tian, B. Wang, Y. Yu, Q. Dong, and D. Xu, “Adaptive active disturbance rejection control for uncertain current ripples suppression of PMSM drives,” *IEEE Trans. Ind. Electron.*, vol. 71, no. 3, pp. 2320–2331, Mar. 2024.

[30] M. Tian, B. Wang, Y. Yu, Q. Dong, and D. Xu, “Robust adaptive resonant controller for PMSM speed regulation considering uncertain periodic and aperiodic disturbances,” *IEEE Trans. Ind. Electron.*, vol. 70, no. 4, pp. 3362–3372, Apr. 2023.

[31] B. Wang, M. Tian, Y. Yu, Q. Dong, and D. Xu, “Enhanced ADRC with quasi-resonant control for PMSM speed regulation considering aperiodic and periodic disturbances,” *IEEE Trans. Transport. Electrific.*, vol. 8, no. 3, pp. 3568–3577, Sep. 2022.

[32] Z. Zhou, C. Xia, Y. Yan, Z. Wang, and T. Shi, “Disturbances attenuation of permanent magnet synchronous motor drives using cascaded predictive-integral-resonant controllers,” *IEEE Trans. Power Electron.*, vol. 33, no. 2, pp. 1514–1527, Feb. 2018.

[33] C. Xia, B. Ji, and Y. Yan, “Smooth speed control for low-speed high-torque permanent-magnet synchronous motor using proportional–integral–resonant controller,” *IEEE Trans. Ind. Electron.*, vol. 62, no. 4, pp. 2123–2134, Apr. 2015.

[34] A. G. Yepes, F. D. Freijedo, Ã. Lopez, and J. Doval- Gandoy, “High-performance digital resonant controllers implemented with two integrators,” *IEEE Trans. Power Electron.*, vol. 26, no. 2, pp. 563–576, Feb. 2011.

[35] C. Boshi, *Electric Drag Automatic Control System: Motion Control System*. South Norwalk, CT, USA: Machinery Ind. Press, 2003.

[36] P. Chen and Y. Luo, “Analytical fractional-order PID controller design with Bode’s ideal cutoff filter for PMSM speed servo system,” *IEEE Trans. Ind. Electron.*, vol. 70, no. 2, pp. 1783–1793, Feb. 2023.

[37] P. Chen, Y. Luo, W. Zheng, Z. Gao, and Y. Chen, “Fractional order active disturbance rejection control with the idea of cascaded fractional order integrator equivalence,” *ISA Trans.*, vol. 114, pp. 359–369, 2021.

[38] Y. Du, W. Cao, and J. She, “Analysis and design of active disturbance rejection control with an improved extended state observer for systems with measurement noise,” *IEEE Trans. Ind. Electron.*, vol. 70, no. 1, pp. 855–865, Jan. 2023.

[39] C. Kim and D. Y. Lee, “An empirical model of friction force between a needle and soft tissue,” in *Proc. 55th Annu. Conf. Soc. Instrum. Control Engineers Jpn.*, 2016, pp. 1692–1697.

[40] K. Johanastrom and C. Canudas-De-Wit, “Revisiting the LuGre friction model,” *IEEE Control Syst. Mag.*, vol. 28, no. 6, pp. 101–114, Dec. 2008.

[41] F. Al-Bender, V. Lampaert, and J. Swevers, “The generalized Maxwell-slip model: A novel model for friction simulation and compensation,” *IEEE Trans. Autom. Control*, vol. 50, no. 11, pp. 1883–1887, Nov. 2005.

Pengchong Chen received the B.S. degree in mechanical engineering from Zhengzhou University, Zhengzhou, China, in 2017, and the Ph.D. degree in mechanical science and engineering from the Huazhong University of Science and Technology, Wuhan, China, in 2022.

He is currently a Lecture with the School of Electrical and Information Engineering, Zhengzhou University. His research interests include mechatronics, robotic control, fractional order control, and active disturbance rejection control.

Ying Luo received the Ph.D. degree in control theory and engineering with a joint-Ph.D. program of the South China University of Technology, Guangzhou, China, and Utah State University, Logan, UT, USA, in 2009.

He is currently a Professor at School of Automation Science and Engineering, South China University of Technology, Guangzhou, China. Together with Prof. Yangquan Chen, he authored a research monograph entitled *Fractional Order Motion Controls*. His current research interests include applied fractional calculus in modeling and controls, mechatronics and robotics, motion controls, active disturbance rejection controls, and smart control engineering.

He Gan received the B.E. degree in mechanical engineering from the Wuhan University of Technology, Wuhan, China, in 2021. He is currently working toward the M.E. degree in mechanical science and engineering with the Huazhong University of Science and Technology, Wuhan.

His research interests include mechatronics and fractional-order control.

Yanhong Liu (Member, IEEE) received the B.E. degree in automation from the Zhengzhou University of Light Industry, Zhengzhou, China, in 1992, and the M.E. and Ph.D. degrees in control science and engineering from Tsinghua University, Beijing, China, in 2002 and 2006, respectively.

She is currently a Professor with the School of Electrical and Information Engineering, Zhengzhou University, Zhengzhou, China. Her current research interests include nonlinear system modeling and control, robotic control, and human–robot interactions and collaborations.

Yangquan Chen (Senior Member, IEEE) received the Ph.D. degree in advanced control and instrumentation from Nanyang Technological University, Singapore, in 1998.

He was a Faculty of Electrical Engineering with Utah State University (USU) from 2000 to 2012. He joined the School of Engineering, University of California, Merced (UCM), in 2012. His research interests include mechatronics for sustainability, cognitive process control (smart control engineering enabled by digital twins), small multi-UAS-based cooperative multispectral “personal remote sensing” for precision agriculture and environment monitoring, applied fractional calculus in controls, modeling, and complex signal processing.

Dr. Chen is a recipient of the Outstanding Research of the Year awards from both USU in 2012 and UCM in 2020. He was listed in Highly Cited Researchers by Clarivate Analytics in 2018, 2019, 2020, and 2021.